# Numerical Simulation of Relatively Wide, Shallow Channels with Erodible Banks

Chang-Lae Jang[1] and Yasuyuki Shimizu[2]

**Abstract:** A two-dimensional numerical model was developed to simulate relatively wide, shallow rivers with an erodible bed and banks composed of well-sorted, sandy materials. A moving boundary-fitted coordinate system was used to calculate water flow, bed change, and bank erosion. The cubic interpolated pseudoparticle method was used to calculate flow, which introduced little numerical diffusion. The sediment-transport equation for the streamline and transverse transport was used to estimate bed and bank evolution over time, while considering the secondary flow. Bank erosion was simulated when the gradient in the cross-sectional direction of the banks was steeper than the submerged angle of repose because of bed erosion near the banks. The numerical model reproduced the features of central bars well, such as bar growth, channel widening due to divergence of the flow around the bars, scour holes at the lee of the bars, and the increase of bar size with time. These features were in accordance with the observations for laboratory experiments. It also reproduced the features of braided rivers, such as the generation of new channels and abandonment of old channels, the bifurcation and confluence of channels, and the lateral migration of the channels. The model showed that the sediment discharge rate fluctuated with time, one of the dynamic features observed in braided channels.

**DOI:** 10.1061/(ASCE)0733-9429(2005)131:7(565)

**CE Database subject headings:** Bars; Bank erosion; Numerical models; Channels, waterways; Sediment discharge; Shallow water.

## Introduction

The morphological changes of rivers are deeply interrelated with bed deformation and bank erosion because of the mutual relationship between water flow and sediment transport. A better understanding of these processes is very important in river engineering to prevent disasters due to flooding, to design and manage hydraulic structures, like bridges and water intake towers, and to maintain river ecosystems and the landscape for environmental engineering purposes.

In the process of channel development, bars emerge under certain hydraulic conditions as the channel widens from an initially straight channel, with erodible bed and banks. Previous investigations examined the mechanical processes of channels with erodible banks theoretically (Ikeda et al. 1981; Parker et al. 1982), and have provided a method to reproduce lateral changes in the channel. The model of Ikeda et al. (1981) was improved by Blondeaux and Seminara (1985) by explaining the resonance phenomenon between a bar and a bend in a channel with erodible banks theoretically. This phenomenon results in local bank erosion that depends on the behavior of the bars, and has been found experimentally to lead to a meandering channel because of alternate bars and to a braided channel because of central or double-row bars (Leopold and Wolman 1957; Ashmore 1982, 1991; Fujita 1989; ASCE Task Committee 1998).

Numerical models to reproduce the evolution of meandering channels, taking bank erosion into consideration, have been developed for beds and banks made of uniform (Shimizu et al. 1996; Nagata et al. 2000) and mixed (Sun et al. 2001a,b; Darby et al. 2002) materials.

Recently, several numerical models have been developed to simulate the deformation of a relatively narrow, deep, straight channel with erodible, noncohesive banks in the laboratory (Pizzuto 1990; Kovacs and Parker 1994; Shimizu 2002), and for natural rivers (Darby and Thorne 1996; Darby et al. 1996). Moreover, Pizzuto (1990) showed that the equilibrium depth of stable gravel rivers increased with increasing bank strength. Murray and Paola (1994, 1997) reproduced the spatial and temporal features of braided rivers using a relatively simple cellular numerical model in a fixed grid system. Two-dimensional numerical models have been developed to simulate braided rivers (Enggrob and Tjerry 1999; McArdell and Faeh 2001; Shimizu et al. 2001). However, these models have some limitations when it comes to treating a relatively shallow, wide channel with moving boundaries due to channel widening.

This paper develops a two-dimensional numerical model to simulate the processes of channel evolution from an initially straight channel with a relatively high width-to-depth ratio and erodible banks composed of noncohesive materials. A moving boundary-fitted coordinate system is used to describe a naturally shaped boundary assuming that sediment erosion and deposition take place in the cross-sectional direction. The flow field is calculated using a high-order Godunov scheme, i.e., the cubic interpolated pseudoparticle (CIP) method (Yabe et al. 1990). It is assumed that banks erode when the gradient in the cross-sectional

[1]Senior Researcher, Korea Institute of Water and Environment, KOWACO, 462-1, Jeonmin-dong, Yuseong-gu, Daejeon, 305-730, Korea. E-mail: cljang@kowaco.or.kr

[2]Professor, Division of Environmental and Resource Engineering, Hokkaido Univ., North 13, West 8, Kitaku, Sapporo, Hokkaido, 060-8628, Japan. E-mail: yasu@eng.hokudai.ac.jp

Note. Discussion open until December 1, 2005. Separate discussions must be submitted for individual papers. To extend the closing date by one month, a written request must be filed with the ASCE Managing Editor. The manuscript for this paper was submitted for review and possible publication on August 26, 2002; approved on December 7, 2004. This paper is part of the ***Journal of Hydraulic Engineering***, Vol. 131, No. 7, July 1, 2005. ©ASCE, ISSN 0733-9429/2005/7-565–575/$25.00.

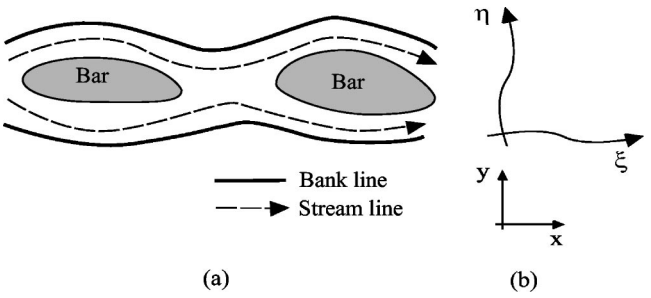


**Fig. 1.** (a) Sketches of a channel and (b) a moving boundary fitted coordinate system

direction of the banks is steeper than the submerged angle of repose because of bed erosion near the banks. The amount of sediment exceeding the submerged critical angle of the bank slope is included in the computation of bed evolution as the supply of sediment from the banks. Conversely, the inner banks at channel bends and other areas, which are transformed into dry land, are successively excluded from the computational range. The model results were compared with laboratory experiments, which demonstrated its applicability.

## Governing Equations

The governing equations, i.e., the continuity and momentum equations, for water flow are transformed from the Cartesian coordinate system to a moving boundary-fitted coordinate system due to the deformation of side banks, as shown in Fig. 1. The equations in the moving boundary-fitted coordinate system are as follows.

The continuity equation:

$$\frac{\partial}{\partial \tau}\left(\frac{h}{J}\right)+\frac{\partial}{\partial \xi}\left[(\xi_t+u^{\xi})\frac{h}{J}\right]+\frac{\partial}{\partial \eta}\left[(\eta_t+u^{\eta})\frac{h}{J}\right]=0 \tag{1}$$

The momentum equations in the $\xi$ and $\eta$ directions:

$$\frac{\partial u^{\xi}}{\partial \tau}+(\xi_t+u^{\xi})\frac{\partial u^{\xi}}{\partial \xi}+(\eta_t+u^{\eta})\frac{\partial u^{\xi}}{\partial \eta}+\alpha_1 u^{\xi}u^{\xi}+\alpha_2 u^{\xi}u^{\eta}+\alpha_3 u^{\eta}u^{\eta}$$
$$=-g\left[(\xi_x^2+\xi_y^2)\frac{\partial H}{\partial \xi}(\xi_x\eta_x+\xi_y\eta_y)\frac{\partial H}{\partial \eta}\right]$$
$$-\frac{C_d u^{\xi}}{hJ}\sqrt{(\eta_y u^{\xi}-\xi_y u^{\eta})^2+(-\eta_x u^{\xi}-\xi_x u^{\eta})^2}+\frac{\partial}{\partial \xi}\left(\nu_t \xi_r^2\frac{\partial u^{\xi}}{\partial \xi}\right)$$
$$+\frac{\partial}{\partial \eta}\left(\nu_t \eta_r^2\frac{\partial u^{\xi}}{\partial \eta}\right) \tag{2}$$

$$\frac{\partial u^{\eta}}{\partial \tau}+(\xi_t+u^{\xi})\frac{\partial u^{\eta}}{\partial \xi}+(\eta_t+u^{\eta})\frac{\partial u^{\eta}}{\partial \eta}+\alpha_4 u^{\xi}u^{\xi}+\alpha_5 u^{\xi}u^{\eta}+\alpha_6 u^{\eta}u^{\eta}$$
$$=-g\left[(\eta_x^2+\eta_y^2)\frac{\partial H}{\partial \eta}(\xi_x\eta_x+\xi_y\eta_y)\frac{\partial H}{\partial \xi}\right]$$
$$-\frac{C_d u^{\eta}}{hJ}\sqrt{(\eta_y u^{\xi}-\xi_y u^{\eta})^2+(-\eta_x u^{\xi}-\xi_x u^{\eta})^2}+\frac{\partial}{\partial \xi}\left(\nu_t \xi_r^2\frac{\partial u^{\eta}}{\partial \xi}\right)$$
$$+\frac{\partial}{\partial \eta}\left(\nu_t \eta_r^2\frac{\partial u^{\eta}}{\partial \eta}\right) \tag{3}$$

where $\xi$ and $\eta$=spatial coordinate components in the boundary-fitted coordinate system; $\tau$=time coordinate (=$t$ in this model) in the coordinate system, $x$ and $y$=spatial coordinate components in the Cartesian coordinate system; $H$=water surface elevation (=$h+z_b$); $h$=water depth; $z_b$=bed elevation referred to a horizontal plane; $g$=gravitational acceleration; $C_d$=bed friction coefficient, which is written using Manning's roughness coefficient as $gn_m^2/h^{1/3}$; $n_m$=Manning's roughness coefficient (=$d^{1/6}/8.9\sqrt{g}$), estimated using Kishi and Kuroki's (1973) formula for flat beds, neglecting the influence of local bed forms; $d$=mean diameter of the bed material; $J$=Jacobian of the coordinate transformation given as $J=\tau_t\xi_x\eta_y+\xi_t\eta_x\tau_y+\eta_t\tau_x\xi_y-(\eta_t\xi_x\tau_y+\xi_t\tau_x\eta_y+\tau_t\xi_y\eta_x)$; $u^{\xi}$ and $u^{\eta}$=contravariant components of the flow velocity in the $\xi$ and $\eta$ directions defined as $u^{\xi}=\xi_x u+\xi_y v$ and $u^{\eta}=\eta_x u+\eta_y v$; $u$ and $v$=depth-averaged velocity components in the $x$ and $y$ directions, respectively. $\xi_r=\Delta\xi/\Delta\tilde{\xi}$ and $\eta_r=\Delta\eta/\Delta\tilde{\eta}$; $\Delta\xi$ and $\Delta\eta$=grid size in the $\xi$ and $\eta$ directions, respectively, in the moving boundary system. $\Delta\tilde{\xi}$ and $\Delta\tilde{\eta}$=local grid size in the system. The coefficients, $\alpha_1$–$\alpha_6$, are given by

$$\alpha_1=\xi_x\frac{\partial^2 x}{\partial \xi^2}+\xi_y\frac{\partial^2 y}{\partial \xi^2} \tag{4}$$

$$\alpha_2=2\left(\xi_x\frac{\partial^2 x}{\partial \xi\,\partial \eta}+\xi_y\frac{\partial^2 y}{\partial \xi\,\partial \eta}\right) \tag{5}$$

$$\alpha_3=\xi_x\frac{\partial^2 x}{\partial \eta^2}+\xi_y\frac{\partial^2 y}{\partial \eta^2} \tag{6}$$

$$\alpha_4=\eta_x\frac{\partial^2 x}{\partial \xi^2}+\eta_y\frac{\partial^2 y}{\partial \xi^2} \tag{7}$$

$$\alpha_5=2\left(\eta_x\frac{\partial^2 x}{\partial \xi\,\partial \eta}+\eta_y\frac{\partial^2 y}{\partial \xi\,\partial \eta}\right) \tag{8}$$

$$\alpha_6=\eta_x\frac{\partial^2 x}{\partial \eta^2}+\eta_y\frac{\partial^2 y}{\partial \eta^2} \tag{9}$$

Assuming a linear distribution of the shear stress, the depth-averaged diffusion coefficient, $\nu_t$, is given as

$$\nu_t=\frac{\kappa}{6}u_* h \tag{10}$$

where $\kappa$=Von Karman constant (=0.4) and $u_*$=shear velocity (=$n_m[g(u^2+v^2)]^{1/2}/h^{1/6}$).

The two-dimensional sediment continuity equation in a moving boundary-fitted coordinate system is

$$\frac{\partial}{\partial t}\left(\frac{z_b}{J}\right)+\frac{1}{1-\lambda}\left[\frac{\partial}{\partial \xi}\left(\frac{q_b^{\xi}}{J}\right)+\frac{\partial}{\partial \eta}\left(\frac{q_b^{\eta}}{J}\right)\right]=0 \tag{11}$$

where $z_b$=bed elevation; $\lambda$=porosity of the bed material; and $q_b^{\xi}$ and $q_b^{\eta}$=contravariant components of the bedload transport rate per unit width in the $\xi$ and $\eta$ directions, respectively.

The sediment-transport rate in the streamline is calculated using Meyer-Peter and Muller's (1948) formula, and given as

$$q_b=8\sqrt{\left(\frac{\rho_s}{\rho}-1\right)gd^3}(\tau_*-\tau_{*_c})^{3/2} \tag{12}$$

where $\rho_s$=density of the bed material; $\rho$=density of water; $\tau_*$=nondimensional shear stress on the bed; and

$\tau_{*_c}$=nondimensional critical shear stress on the bed, obtained using Iwagaki's (1956) formula.

The sediment-transport rate in the $\xi$ direction, $q_b^{\xi}$, is given as (Watanabe et al. 2001)

$$q_b^{\xi} = q_b\left[\frac{u_b^{\xi}}{V_b} - \gamma\left(\frac{\partial z_b}{\partial \xi} + \cos\theta\frac{\partial z_b}{\partial \eta}\right)\right] \tag{13}$$

The sediment-transport rate in the $\eta$ direction, $q_b^{\eta}$, is written as (Watanabe et al. 2001)

$$q_b^{\eta} = q_b\left[\frac{u_b^{\eta}}{V_b} - \gamma\left(\frac{\partial z_b}{\partial \eta} + \cos\theta\frac{\partial z_b}{\partial \xi}\right)\right] \tag{14}$$

where $u_b^{\xi}$ and $u_b^{\eta}$=flow velocity near the bed in the $\xi$ and $\eta$ directions, respectively; $V_b$=resultant velocity near the bed, which is explained below; $\theta$=intersection angle between the $\xi$ and $\eta$ axes; $\gamma=(\tau_{*_c}/\mu_s\mu_k\tau_*)^{1/2}$, as proposed by Hasegawa (1984); $\mu_s$=static coefficient of Coulomb friction (=1.0); and $\mu_k$=dynamic coefficient of Coulomb friction (=0.45).

The near-bed flow velocity in the streamwise direction is assumed to be

$$u_b^s = \beta V \tag{15}$$

where $V$=resultant velocity of depth-averaged flow [$=(u^2+v^2)^{1/2}$].

Assuming a parabolic distribution of flow in the depth-wise direction following Engelund (1974), $\beta$ is written as

$$\beta = 3(1-\sigma)(3-\sigma) \tag{16}$$

where $\sigma=3/(\phi\kappa+1)$; $\phi$=velocity factor ($=V/u_*$); and $\kappa$=Von Karman constant (=0.4).

When the streamline is curved, secondary flow is generated by the variation in the centrifugal force. The near-bed flow velocity perpendicular to the streamwise direction is written as

$$u_b^n = u_b^s N_* \frac{h}{r_s} \tag{17}$$

where $r_s$=radius of curvature of the streamline and $N_*$=coefficient of the strength of the secondary flow, which is assumed to be 7.0, as proposed by Engelund (1974). $V_b$ is written as

$$V_b = \sqrt{(u_b^s)^2 + (u_b^n)^2} \tag{18}$$

and $u_b^{\xi}$ and $u_b^{\eta}$ in Eqs. (13) and (14) are given by

$$u_b^{\xi} = \frac{1}{\xi_r}[(\cos\theta_s\,\xi_x + \sin\theta_s\,\xi_y)u_b^s + (-\sin\theta_s\,\xi_x + \cos\theta_s\,\xi_y)u_b^n] \tag{19}$$

$$u_b^{\eta} = \frac{1}{\xi_r}[(\cos\theta_s\,\eta_x + \sin\theta_s\,\eta_y)u_b^s + (-\sin\theta_s\,\eta_x + \cos\theta_s\,\eta_y)u_b^n] \tag{20}$$

The term on the right-hand side in Eq. (17) is the intensity of secondary flow in a curved streamline due to bank erosion and bed deformation, and the curvature of the streamline, $1/r_s$, is determined by the angle ($=\theta_s$) between the streamline in the main stream direction and the $x$ axis in Cartesian coordinates, as shown in Fig. 2:

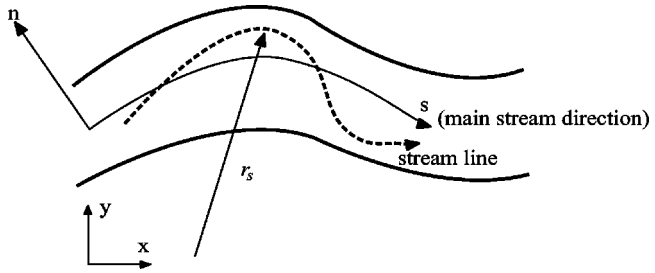


**Fig. 2.** Definition sketch of stream line and radius of curvature ($r_s$)

$$\frac{1}{r_s} = \frac{\partial\theta_s}{\partial s} = \frac{\partial}{\partial s}\left[\tan^{-1}\left(\frac{v}{u}\right)\right] = \frac{\partial}{\partial T}[\tan^{-1}(T)]\frac{\partial T}{\partial s} = \frac{1}{1+T^2}\frac{\partial T}{\partial s} \tag{21}$$

In this equation:

$$T = \frac{v}{u} \tag{22}$$

$$\frac{1}{1+T^2} = \frac{1}{1+\left(\frac{v}{u}\right)^2} = \frac{u^2}{u^2+v^2} = \frac{u^2}{V^2} \tag{23}$$

$$\frac{\partial T}{\partial s} = \frac{\partial}{\partial s}\left(\frac{v}{u}\right) = \frac{u\frac{\partial v}{\partial s} - v\frac{\partial u}{\partial s}}{u^2} \tag{24}$$

$$\frac{\partial}{\partial s} = \frac{\partial x}{\partial s}\frac{\partial}{\partial x} + \frac{\partial y}{\partial s}\frac{\partial}{\partial y} = \frac{u}{V}\frac{\partial}{\partial x} + \frac{v}{V}\frac{\partial}{\partial y} = \frac{u}{V}\left(\xi_x\frac{\partial}{\partial \xi} + \eta_x\frac{\partial}{\partial \eta}\right) + \frac{v}{V}\left(\xi_y\frac{\partial}{\partial \xi} + \eta_y\frac{\partial}{\partial \eta}\right) \tag{25}$$

where $V=\sqrt{(u^2+v^2)}$.

According to Eq. (25), the curvature of streamline, $r_s$, in the moving boundary-fitted coordinate system is given by

$$\frac{1}{r_s} = \frac{1}{V^3}\left[u^2\left(\xi_x\frac{\partial v}{\partial \xi} + \eta_x\frac{\partial v}{\partial \eta}\right) + uv\left(\xi_x\frac{\partial v}{\partial \xi} + \eta_y\frac{\partial v}{\partial \eta}\right) - uv\left(\xi_x\frac{\partial u}{\partial \xi} + \eta_x\frac{\partial u}{\partial \eta}\right) - v^2\left(\xi_y\frac{\partial u}{\partial \xi} + \eta_y\frac{\partial u}{\partial \eta}\right)\right] \tag{26}$$

The nondimensional bed shear stress, $\tau_*$, in Eq. (12), is given by

$$\tau_* = \frac{C_d V^2}{\left(\frac{\rho_s}{\rho} - 1\right)gd} = \frac{C_d(u^2+v^2)}{\left(\frac{\rho_s}{\rho} - 1\right)gd} \tag{27}$$

where $C_d$=bed friction coefficient and $d$=mean diameter of the bed material.

## Numerical Method

The governing equations, i.e., the continuity and momentum equations, for water flow are calculated numerically using the finite difference method with computational grids in $(\xi,\eta)$ coordinate systems. To solve Eqs. (2) and (3), a high-order Godunov scheme known as the cubic interpolated psuedoparticle (CIP)

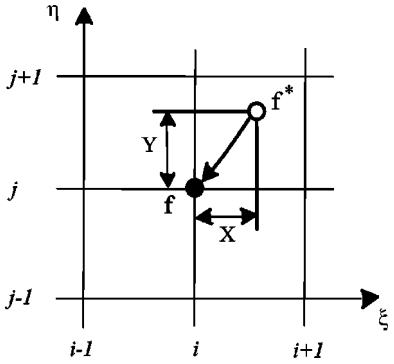


**Fig. 3.** Conceptual diagram of the cubic interpolated pseudoparticle method used in the computational domain

method, proposed by Yabe et al. (1990), is used. It is assumed that at very small time increments, the temporal change in the velocity components at a point can be broken down into the time evolution of the nonhomogeneous terms and the time evolution at a point due to the advection of the field. Fig. 3 shows the conceptual diagram of the CIP method in the computational domain. Therefore, in the first step, the temporal change of the velocity ($u^{\xi}$ and $u^{\eta}$ denoted here as $f$) is solved as

$$\frac{\partial f^*}{\partial t} = G \tag{28}$$

where $f^*$=value at points in space which do not lie on the numerical grid points and $G$=sum of the nonadvection terms in Eqs. (2) and (3). Then, $f$ is solved in the advection phase as

$$\frac{\partial f}{\partial \tau} + \tilde{u}\frac{\partial f}{\partial \xi} + \tilde{v}\frac{\partial f}{\partial \eta} = 0 \tag{29}$$

where $\tilde{u}=\xi_t+u^{\xi}$ and $\tilde{v}=\eta_t+u^{\eta}$. The solution of Eq. (29) for small $\Delta\tau$ is simply approximated as

$$f(\xi,\eta,\tau+\Delta\tau) \approx f(\xi-\tilde{u}\Delta\tau,\eta-\tilde{v}\Delta\tau,\tau) \tag{30}$$

Using the solution of the nonadvection phase, Eq. (28), this approximation becomes

$$f(\xi,\eta,\tau+\Delta\tau) = f^*(\xi-\tilde{u}\Delta\tau,\eta-\tilde{v}\Delta\tau,\tau+\Delta\tau) \tag{31}$$

Then, the method finds the value of $f^*$ at points in space that generally do not lie on the numerical grid points, as specified by the right-hand side of Eq. (31). If linear interpolation is used to find $f^*$ at points not on the grid, this is the first-order Godunov method. A more accurate solution requires higher-order interpolation, that is, high-order Godunov schemes. The CIP method proposes a cubic interpolation of $f^*$, and when the interpolation is combined with Eq. (31), the resultant equation for $f$ at grid point $(i,j)$ and time $n+1$ is given by

$$f_{i,j}^{n+1} = [(a_1X + c_1Y + e_1)X + g_1Y + f_{\xi}^*(i,j)]X + [(b_1Y + d_1X + f_1)Y + f_{\eta}^*(i,j)]Y + f^*(i,j) \tag{32}$$

where

$$X = -\tilde{u}\Delta\tau, \quad Y = -\tilde{v}\Delta\tau \tag{33}$$

$$f_{\xi}^* = \frac{\partial f^*}{\partial \xi}, \quad f_{\eta}^* = \frac{\partial f^*}{\partial \eta} \tag{34}$$

$$a_1 = \{[f_{\xi}^*(i+1,j) + f_{\xi}^*(i,j)]\Delta\xi + 2[f^*(i,j) - f^*(i+1,j)]\}/(\Delta\xi^3) \tag{35}$$

$$b_1 = \{[f_{\eta}^*(i,j+1) + f_{\eta}^*(i,j)]\Delta\eta + 2[f^*(i,j) - f^*(i,j+1)]\}/(\Delta\eta^3) \tag{36}$$

$$c_1 = \{f^*(i,j) - f^*(i,j+1) - f^*(i+1,j) + f^*(i+1,j+1) - [f_{\xi}^*(i,j+1) - f_{\xi}^*(i,j)]\Delta\xi\}/(\Delta\xi^2\Delta\eta) \tag{37}$$

$$d_1 = \{f^*(i,j) - f^*(i,j+1) - f^*(i+1,j) + f^*(i+1,j+1) - [f_{\eta}^*(i+1,j) - f_{\eta}^*(i,j)]\Delta\eta\}/(\Delta\xi\Delta\eta^2) \tag{38}$$

$$e_1 = \{3[f^*(i+1,j) - f^*(i,j)] - [f_{\xi}^*(i+1,j) + 2f_{\xi}^*(i,j)]\Delta\xi\}/\Delta\xi^2 \tag{39}$$

$$f_1 = \{3[f^*(i,j+1) - f^*(i,j)] - [f_{\eta}^*(i,j+1) + 2f_{\eta}^*(i,j)]\Delta\eta\}/\Delta\eta^2 \tag{40}$$

$$g_1 = [-f_{\eta}^*(i+1,j) + f_{\eta}^*(i,j) - c_1\Delta\xi^2]/\Delta\xi \tag{41}$$

In the previous instance, it is assumed that $\tilde{u}$ and $\tilde{v}$ are negative, so that the advection to grid point $(i,j)$ is from within the area bounded by the vertices $(i,j)$, $(i+1,j)$, $(i,j+1)$, and $(i+1,j+1)$. When $\tilde{u}\geq 0$, the term $i+1$ in Eqs. (35)–(41) should be changed to $i-1$, and $\Delta\xi$ becomes $-\Delta\xi$. Similarly, when $\tilde{v}\geq 0$, $j+1$ and $\Delta\eta$ become $j-1$ and $-\Delta\eta$, respectively. In the nonadvection phase, $f^*$ is calculated from the continuity equation by taking the divergence of the momentum equations and solving for depth as a Poisson equation. The viscous terms are approximated using the central difference method. Each velocity component is defined in the center of two faces of the computational cells, and depth is defined at the center of the cell. The general procedure is to calculate $f^*$ from Eq. (28), in which the convective acceleration terms do not appear. In the second phase, $f$ is calculated at the grid points from a pure advection of the cubic interpolated field of $f^*$ using Eqs. (32)–(41). These two steps complete the calculation for a single time increment, $\Delta\tau$. The CIP method solves boundary problems while introducing little numerical diffusion, and algorithm implementation is more straightforward than for other high-order upwind schemes (Yabe and Aoki 1991; Yabe et al. 1991).

### Bank Erosion and Channel Migration

The $\xi$ axis is drawn along the channel for a given initial channel with a plane shape, and the $\eta$ axis is set to intersect the $\xi$ axis. Then, the plane $(\xi,\eta)$ is divided into the parts to form the initial grid for the computations. The flow and bed evolution are computed using the governing equations described in the previous sections. With special attention to the bed evolution near the banks, the deformation in the plane shape of the channel is calculated in the following manner.

To calculate bank erosion, when the riverbed near the banks is scoured [Fig. 4(a-1)] and the cross-sectional gradient of the bank slope becomes steeper than the submerged angle of repose ($\theta_c$), it is assumed that any sediment beyond the submerged angle of repose is instantly eroded to the point of this submerged angle of repose [Fig. 4(a-1)] (Hasegawa 1984). Further, it is assumed that the sediment load equal to the amount of sediment beyond the submerged angle of repose is deposited at the toe of the bank slope [Fig. 4(a-1)]. At this time, if the erosion of the bank slope

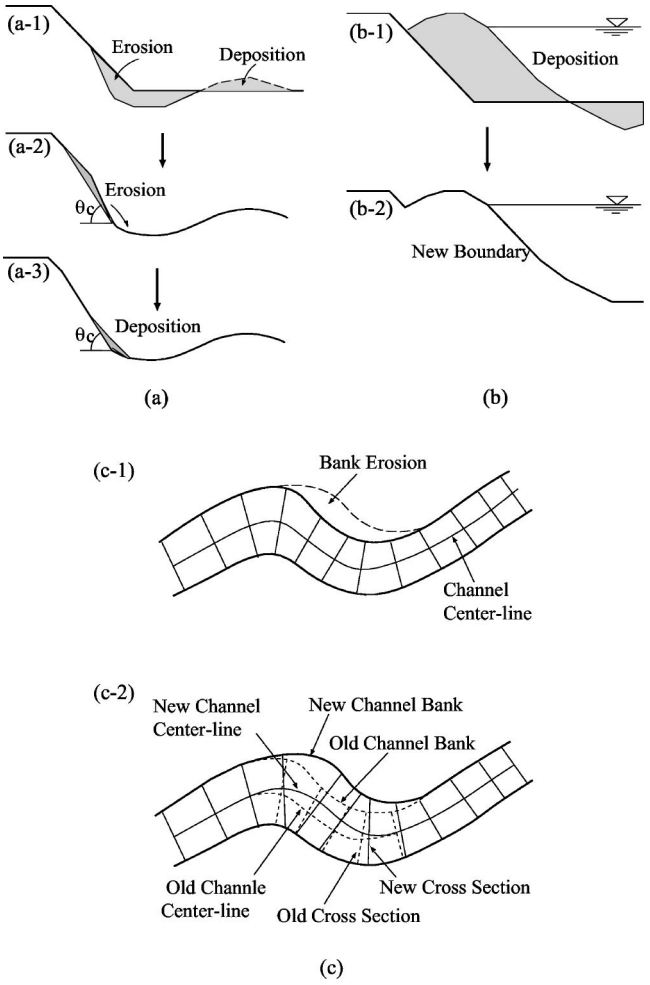


**Fig. 4.** Bed deformation and the renewal of channel geometry: (a) Bed degradation and bank erosion; (b) bed aggradation and bank deposition; and (c) bank deformation and renewal of the computational grid aggradation

face advances toward the top of the slope, the computational range is enlarged in the cross-sectional direction of the channel. Moreover, if part of the bed near the bank is transformed into land, narrowing the water channel, the computational range is moved to the new waterline [Fig. 4(b)]. When the computational range is enlarged, for example, due to erosion of the banks [Figs. 4(c-1) and (c-2)], (1) a new central line of the channel passing through the center of new bank lines is set; (2) along this new central line of the channel, new cross-sections perpendicular to this line are set at equal intervals as the initial condition in the $\eta$ direction; and (3) each cross section is divided into grid numbers in the $\xi$ direction. Consequently, new computational meshes are formed, and all the computational data are transformed from the old to the new computational grid. During transformation of all the computational data between the old and new grids, a linear transformation based on geometric locations must be carried out. These calculations are done at intervals of an infinitesimal time ($\Delta t$) and are continued up to a designated time. Note that the values of $\xi_t$ and $\eta_t$ are calculated through these processes and fed back to the Eqs. (1)–(3). In this study, the submerged angle of repose ($\theta_c$) is assumed to be 32.0°.

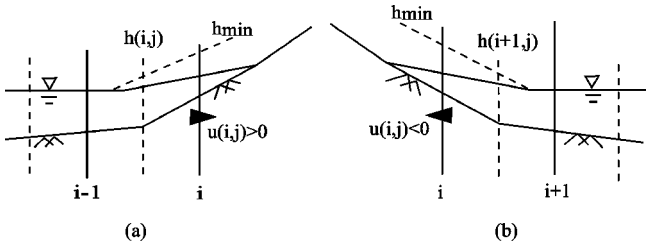


**Fig. 5.** Scheme of boundary near the emerged bars and banks in a staggered grid system: (a) $dh/d\xi<0$ and $u>0$, or $dh/d\eta<0$ and $v>0$ in the longitudinal or transverse direction and (b) $dh/d\xi>0$ and $u<0$, or $dh/d\eta>0$ and $v<0$ in the longitudinal or transverse direction

### Boundary Conditions

To solve the flow equation, a specified discharge, the flow velocity in the streamwise ($u$) and transverse ($v=0$) directions at the upstream end and a specified water depth downstream are given as the boundary conditions. The bottom elevations upstream ($i=1$, 2, and 3) conform to the experimental condition and those downstream are fixed for the bed. At the sidewalls of emerged bars and banks, the no-slip condition is used in the transverse direction and a slip velocity is adopted in the streamwise direction.

Dealing with a partially drying or wetting boundary is important to simulate the inundation of flood plains and wetlands, shallow flows over and near islands or emerged bars in rivers, and wave run-up in a coastal line (Bradford and Sanders 2002; Zhao et al. 1994). Referring to Fig. 5, the boundary in the shallow regions around emerged bars and near side banks with a moving boundary is dealt with as follows.

In the flow direction, near the emerged bars:

$$\text{If} \quad \frac{dh}{d\xi} < 0 \text{ and } u_{i,j} > 0, \quad \text{then } u_{i,j} = 0 \tag{42}$$

$$\text{If} \quad \frac{dh}{d\xi} > 0 \text{ and } u_{i,j} < 0, \quad \text{then } u_{i,j} = 0 \tag{43}$$

In the transverse direction, near emerged bars and side banks:

$$\text{If} \quad \frac{dh}{d\eta} < 0 \text{ and } v_{i,j} > 0, \quad \text{then } v_{i,j} = 0 \tag{44}$$

$$\text{If} \quad \frac{dh}{d\eta} > 0 \text{ and } v_{i,j} < 0, \quad \text{then } v_{i,j} = 0 \tag{45}$$

Since $h_{\min}$ has a very small value, but there is flow velocity in the streamwise or transverse directions in these situations, the momentum equations are not solved and the flow velocity is set to zero, which probably leads to some numerical error, and must be studied further in the future. In these equations, $h_{\min}$ is set to 0.02 mm to minimize the error. In the fully wetted regions, the continuity and momentum equations are solved using the CIP method in the advection terms.

### Computational Procedures

The computational model applies the following process to calculate the changes in flow and the shape of a channel with time at infinitesimal intervals up to the designated time for the given initial conditions:

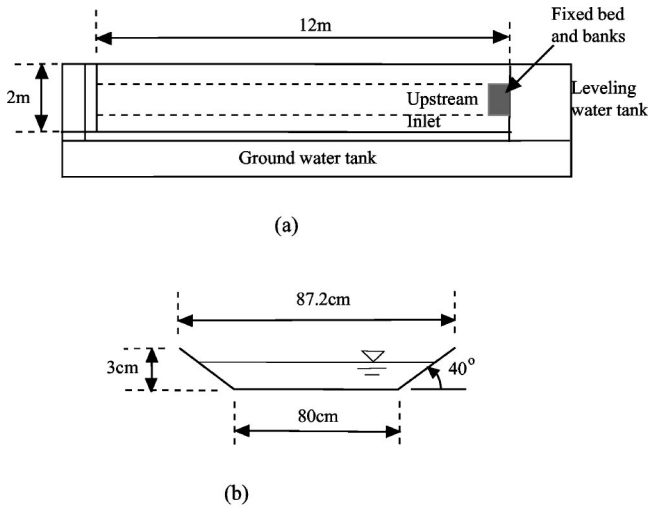


**Fig. 6.** Diagram of experimental setup: (a) Plan view and (b) initial cross section

1. Compute the depth-averaged flow field in the given plane shape of the water channel;
2. Compute the secondary flow perpendicular to the streamline of the depth-averaged flow;
3. Compute the sediment-transport rate and riverbed evolution;
4. Determine how bank erosion and sediment deposition alter the shape of a channel;
5. Set a coordinate system using the new boundary and update the computational data; and
6. Update the time.

## Experimental and Numerical Results

### *Experimental Procedure*

Laboratory experiments were carried out in a flume 12 m in length and 2 m in width, with wooden sidewalls. The flume was filled with well-sorted sand with a mean diameter of 1.25 mm. An initial channel was set with a trapezoidal shape that was 80 cm wide at the bottom, 3 cm high, and had 40° bank slopes, as shown in Fig. 6. A channel with a fixed bed and banks 60 cm in length and 80 cm wide was installed to reduce local scouring at the entrance of flow. The water discharge was controlled to 4.5 and 3.5 L/s under the initial conditions. The nondimensional channel (width/depth ratio) was 59.1 and 89.9, respectively. The experimental conditions are summarized in Table 1.

Sediments were fed by hand regularly at the upstream end of the channel to maintain the channel shape without local disturbance during the experiments. The bed was graded to the intended slope using a wide scraper and the initial channel was cut with a wooden form attached to the lower end of the scraper. Before starting the experiments, some water was allowed to flow over the bed to saturate the bed surface. The water depth was checked at some places using a point gauge after 15 min of flow. Sediment discharge was collected using a sand trapper at the downstream end of the channel. A plastic screen was set to maintain nearly steady-state inflow into the channel in the front of the channel inlet, and the water depth was regulated using a sluice gate to minimize the outlet effect at the downstream end of the channel. The bed configuration was measured using a laser bed profiler without water flow.

**Table 1.** Experimental Conditions

| Run | Mean diameter in the bed material (mm) | Initial slope (%) | Water discharge (L/s) | Initial water depth (cm) | Width/depth |
|---|---|---|---|---|---|
| 1 | 1.25 | 1.0 | 4.5 | 1.41 | 59.1 |
| 2 | 1.25 | 1.5 | 3.5 | 0.93 | 89.9 |

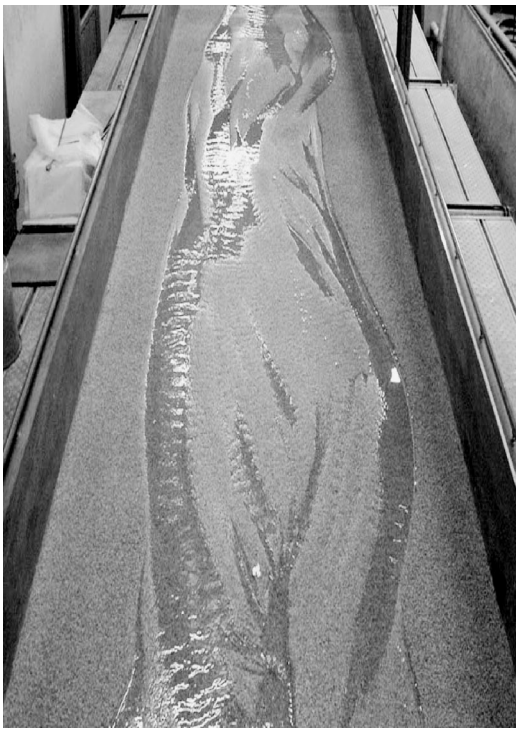

**Fig. 7.** Development from a straight channel into a channel with central bar channel. Experimental result for Run 2 after stopping water flow momentarily. Run time is 95 min. Flow is from top to bottom.

The longitudinal bed profile was measured in the experimental reach from 3 to 10 m from the upstream every 20 cm. The transverse bed profile was surveyed between 0.05 and 1.95 m every 1 cm due to the movement limitations of the profiler.

The experiment for Run 1 was carried out using the initial conditions in which the channel width-to-depth ratio corresponded to the transition regime (aspect ratio = 59.1) between alternate bars and braided bars. For Run 2, the conditions corresponded to the condition for braided bars (aspect ratio = 89.9), according to the regime criteria of Kuroki and Kishi (1984) for bars and braids in straight alluvial channels in the space given by a dimensionless tractive force, where the channel width-to-depth ratio considers the channel slope. One of the experimental results is shown in Fig. 7.

### *Numerical Results*

Numerical calculations were made for an initially straight channel that was 15 m long and 0.8 m in bottom width, with erodible banks. The computational reach was 15.5 m, which was longer than the experimental flume (12 m) to ensure sufficient channel evolution. The computational time step was 0.05 s and there were

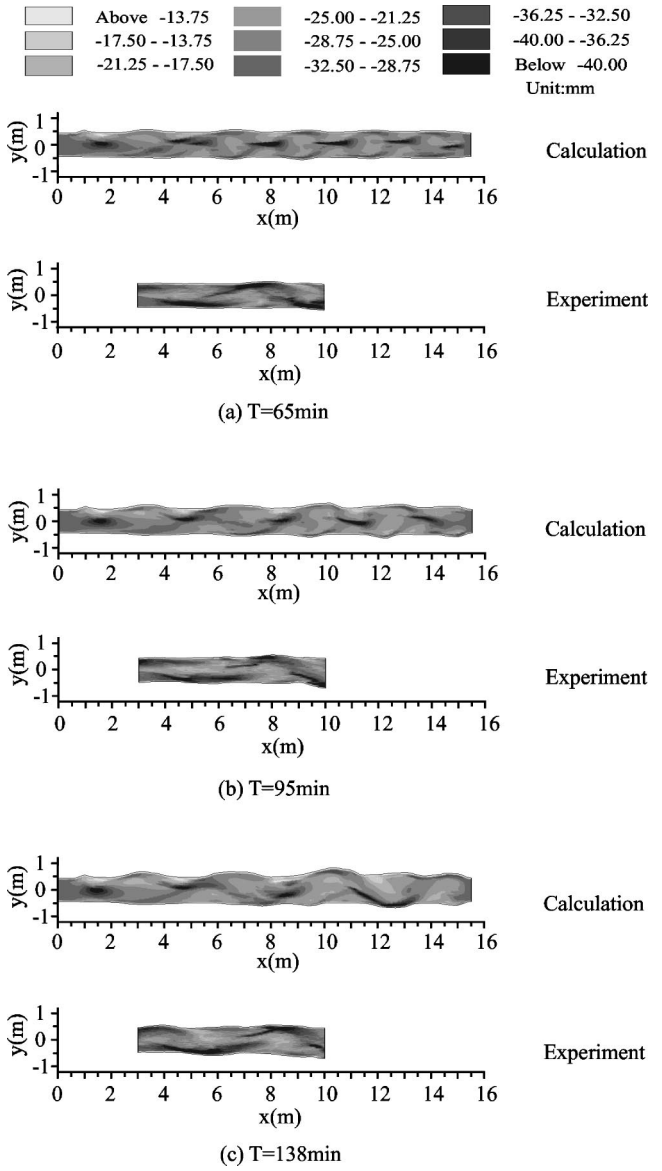


**Fig. 8.** Comparison of channel evolution between numerical and experimental results for Run 1. Flow is from left to right.

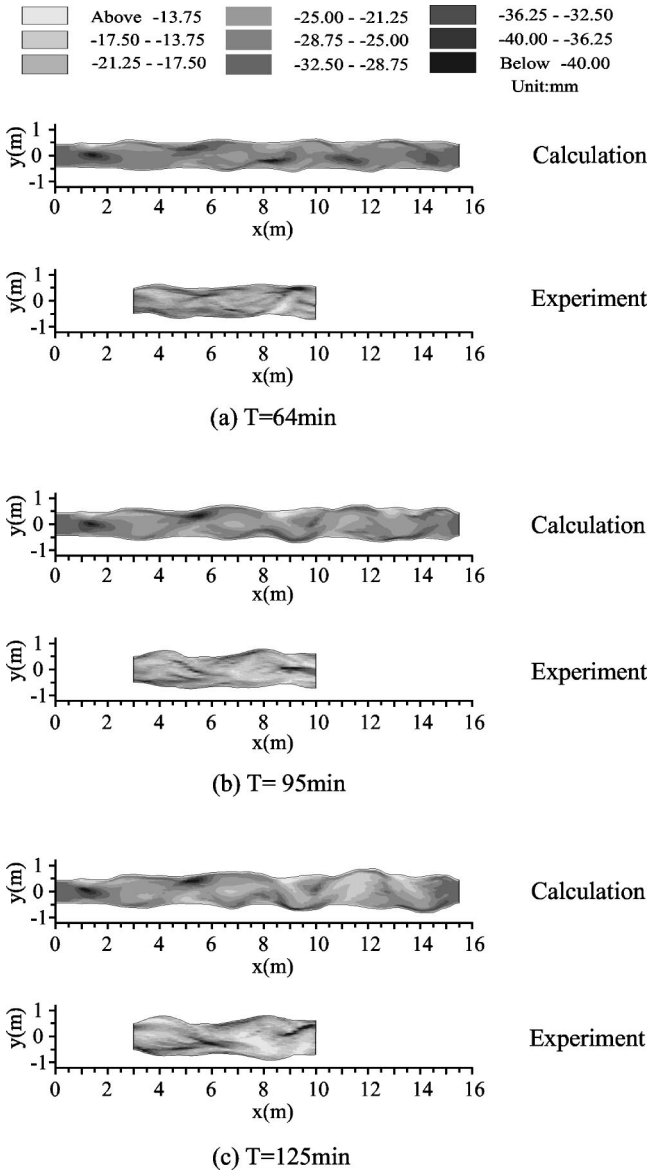


**Fig. 9.** Comparison of channel evolution between numerical and the experimental results for Run 2. Flow is from left to right.

90 grid points in the streamwise direction and 40 in the transverse direction. A rectangular bump, which was 24 cm wide, 1.7 m long, and 1.2 mm high, was introduced as an initial perturbation at the center of the upstream end of the initial channel bed to encourage the development of bars, although the experiment channels were flat.

Figs. 8 and 9 show the numerical and experimental results for Runs 1 and 2. The initially straight channel widened, and central bars were generated and grew due to stalling of the bed load (Ashmore 1991), as shown in Fig. 8(a). The size of the bars increased with time. The bars altered the flow direction, which led to bank erosion around the bars. Side banks eroded due to the flow division around the central bars as time increased. The bed was deeply scoured due to the strong secondary flow driven by the helical vortex at the lee of the bar, which is the confluence point of the flow. The confluence and divergence of flow are also fundamental components of a braided river.

The numerical and experimental results show that asymmetric central bars grow upstream [see Figs. 8(a) and 9(a)]. As time progressed, alternate bar patterns were developed downstream [see Figs. 8(c) and 9(c)] due to the asymmetric bars upstream. The features of the central bar were confirmed by the observations of Federici and Paola (2003) in laboratory experiments. Wavelength, the distance between the confluences of flow to the lee of the bars, was 3.0 m numerically and 2.7 m experimentally for Run 1, and 3.3 and 3.2 m, respectively, for Run 2, as shown in Fig. 10. The difference between the numerical and experiment results is probably due to the fact that the numerical model does not simulate the three-dimensional flow structure at the confluence of the flow, the numerical method used to partially treat wetting or drying boundaries cannot exactly account for the experimental flume, and the numerical model does not exactly reflect unavoidable experimental error, e.g., water pump conditions and flow perturbation at the entrance of flow when the sand was fed, etc. The assumed parameters and initial conditions of the numerical model may be one cause of the differences. Nevertheless, the numerical results are in relatively good agreement with the experimental data.

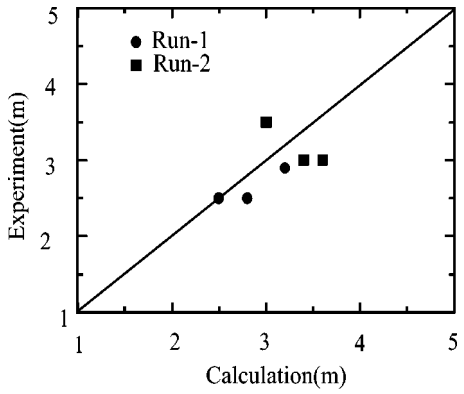


**Fig. 10.** Comparison of the wavelength between calculations and experiments

The simulated and experimental averaged channel widths were compared for each run to investigate channel adjustment, as shown in Fig. 11. The simulated channel width was within 8.6% of the experimental results for Run 1, which was a low widening rate, and 11% for Run 2, which was the high widening rate. The comparison of the calculated and observed averaged channel widths showed that the numerical model simulated channel adjustment well.

The numerical model reproduced the features of central bars well, such as bar growth, channel widening due to the divergence

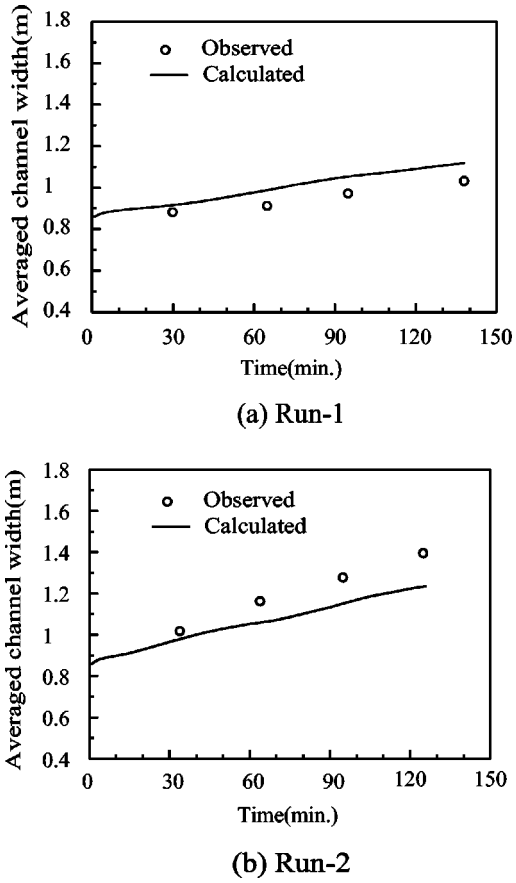


**Fig. 11.** Comparison of the numerical and experimental results for the averaged channel width

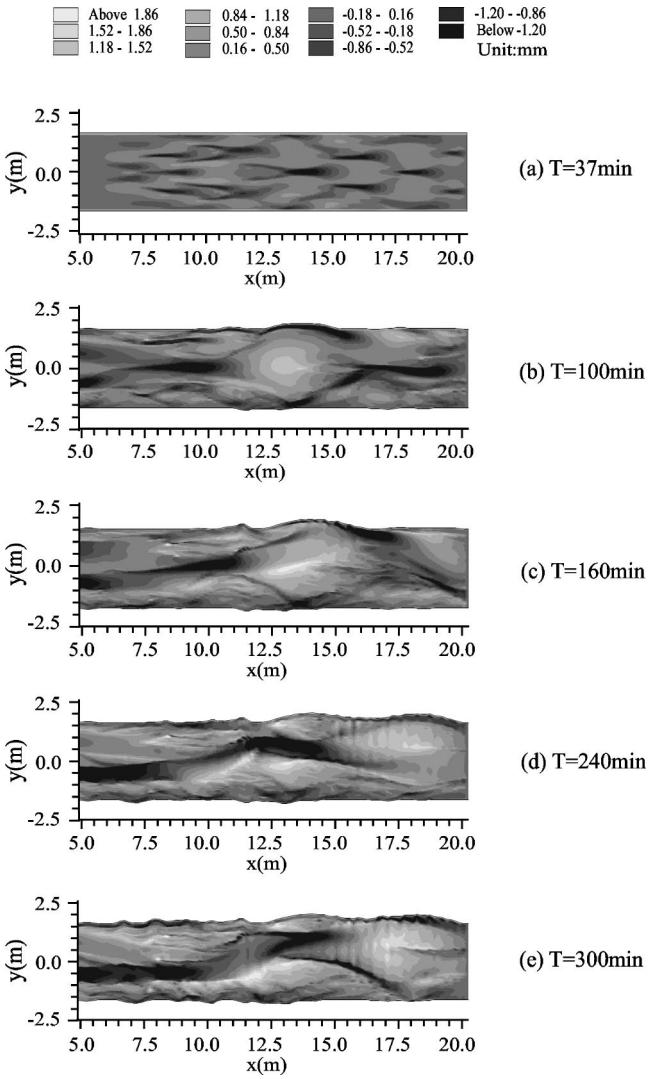


**Fig. 12.** Simulated braided river. Flow is from left to right.

of flow around the bars, scour holes to the lee of the bars, and increasing the bar size with time. These were in accord with the observations in the laboratory experiments.

To investigate the applicability of the numerical model and the evolution processes of braided rivers under the hydraulic condition of larger aspect ratio (width-to-depth ratio) than those used in the experiments, the model was applied to a straight channel with erodible banks that was 20 m long and 3 m wide at the bottom. To the best of our knowledge, there are no experimental data at the large scale. The discharge was 12.0 L/s, and the aspect ratio was 349, i.e., a shallow and wide channel. The computational time step was 0.05 s and there were 120 grid points in the streamwise direction and 80 in the transverse direction. A rectangular bump, which was 96 cm wide, 0.84 m long, and 0.9 mm high, was located at the center of the upstream in the initial channel bed to encourage the development of bars.

Fig. 12 shows the development of a braided river. Submerged multiple row bars developed and migrated to the downstream during the initial stage of the development [Fig. 12(a)]. As shown in Fig. 12(b), the multiple bars merged into large, emerged bars, which strongly deflected flow, leading to channel networks. At the confluence of channels, the bed was scoured deeply by the strong secondary flow. The bank lines became irregular, due to the se-

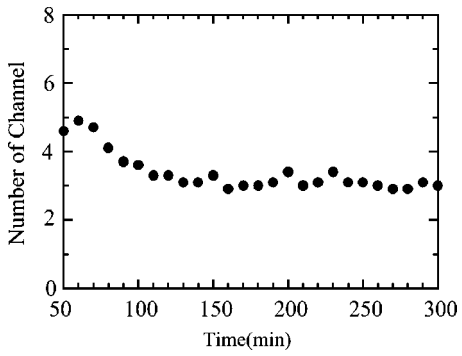


**Fig. 13.** Average number of streams per the width of the braided river with time

lective erosion. Channels migrated laterally in the downstream as shown in Fig. 12(c). In the midstream, new channels were generated, whereas in the downstream old channels were degenerated [Fig. 12(d)]. As time progressed, re-networked channels appeared midstream [Fig. 12(e)].

Fig. 13 shows the average number of streams across the width of the braided channel with time. The number gradually decreased to 140 min. After that, it remained at an asymptotic value of three channels. Fig. 14 shows the number of scour holes with time. The number of holes showed the same pattern as the number of streams. After 140 min, it became approximately six with a little fluctuation.

Fujita (1989) observed the similar process of channel development in shallow, wide laboratory channels without bank erosion (see Runs C-3, 8, and 10). In the early stage, numerous multiple row bars were developed, and then changed to fewer large scale irregular bars along the faces of the bars due to the flow concentrating into scour holes. As time progressed, several small streams were divided into emerged bars, and finally developed to a braided channel.

Fig. 15(a) shows the temporal fluctuation of sediment discharge rate at the end of channel. The averaged sediment discharge rate was 0.037 $m^3$/min and the inflow rate upstream was 0.0024 $m^3$/min. The sediment discharge rate was stable during the initial stage of multiple row bar development (20 min). After braided bars fully developed, the sediment discharge rate fluctuated with sudden increase at 170 and 250 min. Fig. 15(b) illustrates the change of averaged bed elevation with time. The bed elevation decreased slightly to 100 min, and then increased gradually with periodic fluctuation, due to the changes in the sediment inflow rate from the eroding side banks. Moreover, the turning

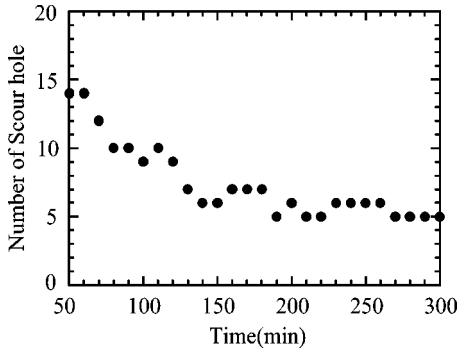


**Fig. 14.** Number of scour holes of the braided river with time

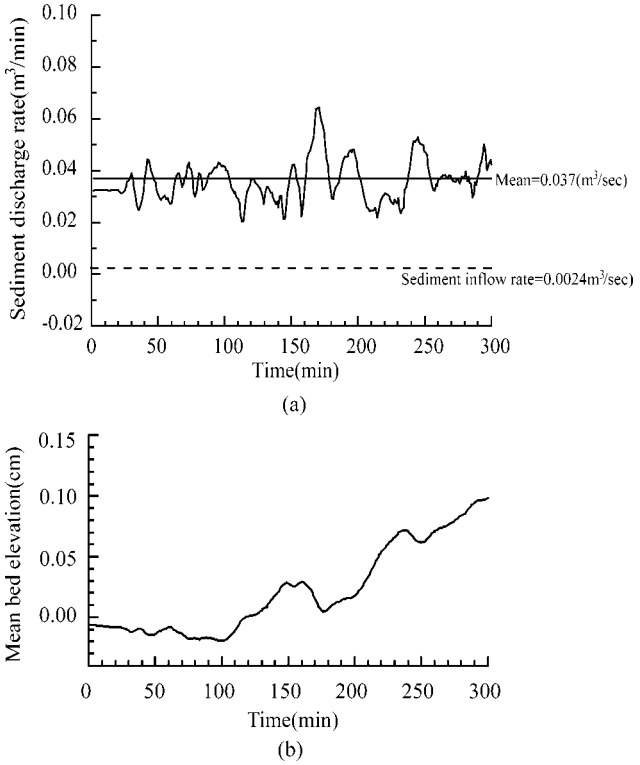


**Fig. 15.** (a) Sediment discharge rate at the end of the channel and (b) average bed elevation with time

point of the bed change rate from down to up at 175 and 250 min approximately corresponded to the big sediment discharge rate as shown in Fig. 15(a). The simulation results showed that the sediment discharge rate fluctuated with time, which is one of the dynamic features observed in braided channels caused by the morphological changes and bar migration (Ashmore 1988, 2001; Hoey and Sutherland 1991).

## Summary

This paper used a model of braided river with erodible banks to estimate channel evolution quantitatively. A moving boundary-fitted coordinate system was used to produce a naturally shaped boundary, because erosion and deposition occurred laterally, and the channel shapes were transformed into arbitrary shapes. The numerical method used the cubic interpolated pseudoparticle method in the flow field, since the method introduced little numerical diffusion. The sediment-transport equation in the streamline and transverse directions, considering secondary flow, was employed to estimate bed and bank evolution with time. Channel widening was simulated using a relatively simple bank erosion concept, i.e., it occurred when the gradient of the bank in the transverse direction exceeded the angle of repose because the bed was scoured near the bank due to secondary flow, leading to a channel with naturally shaped boundary.

The numerical model reproduced the features of central bars well, such as bar growth, channel widening due to the divergence of flow around the bars, scour holes to the lee of the bars, and increasing bar size with time. They were in accordance with the observations of the laboratory experiments. It also reproduced the features of braided rivers, such as the generation of new channels and abandonment of old channels, the bifurcation and confluence

of channels, and the lateral migration of channels. The model showed that temporal fluctuation in the sediment-discharge rate, one of the dynamic features observed in braided channels, was influenced by the bed change.

## Notation

*The following symbols are used in this paper:*

$C_d$ = bed friction coefficient;
$d$ = mean diameter of the sediment;
$f$ = value of $u^{\xi}$ and $u^{\eta}$ on the numerical grid points;
$f^*$ = value at points in space which generally do not lie on the numerical grid points;
$G$ = summation of nonadvection terms;
$g$ = gravitational acceleration;
$H$ = water surface elevation;
$h$ = water depth;
$J$ = Jacobian of the coordinate transformation;
$N_*$ = coefficient of strength of secondary flow (=7.0);
$n_m$ = Manning's roughness coefficient;
$q_b^{\eta}$ = bed load transport rate in the $\eta$ direction;
$q_b^{\xi}$ = bed load transport rate in the $\xi$ direction;
$r_s$ = radius of curvature of a streamline;
$u, v$ = depth-averaged flow velocity components in $x$ and $y$ directions;
$u_b^n$ = flow velocity near the bed perpendicular to the streamwise direction ($n$);
$u_b^s$ = flow velocity near the bed in the streamwise direction(s);
$u^{\eta}$ = flow velocity in the $\eta$ direction;
$u_b^{\eta}$ = flow velocity near the bed in the $\eta$ direction;
$u^{\xi}$ = flow velocity in the $\xi$ direction;
$u_b^{\xi}$ = flow velocity near the bed in the $\xi$ direction;
$u_*$ = shear velocity;
$V$ = resultant velocity of depth-averaged flow ($=\sqrt{u^2+v^2}$);
$V_b$ = resultant velocity near bed ($=\sqrt{(u_b^s)^2+(u_b^n)^2}$);
$x, y$ = coordinate components in the Cartesian coordinate system;
$z_b$ = bed elevation referred to a horizontal plane;
$\Delta t$ = computational time interval;
$\Delta\eta$ = grid size in the $\eta$ direction;
$\Delta\xi$ = grid size in the $\xi$ direction;
$\theta_c$ = submerged angle of repose;
$\theta_s$ = angle between the stream line in the main stream direction ($s$) and the $x$ axis in the Cartesian coordinate;
$\kappa$ = Von Karman constant (=0.4);
$\lambda$ = porosity of the bed material;
$\mu_k$ = dynamic coefficient of Coulomb coefficient (=0.45);
$\mu_s$ = static coefficient of Coulomb coefficient (=1.0);
$\nu_t$ = depth-averaged diffusion coefficient;
$\xi, \eta$ = coordinate components in the moving boundary-fitted coordinate system;
$\rho$ = density of water;
$\rho_s$ = density of the bed material;
$\tau$ = time coordinate in the moving boundary-fitted coordinate system;
$\tau_*$ = nondimensional shear stress on the bed;
$\tau_{*_c}$ = nondimensional critical shear stress on the bed; and
$\phi$ = velocity factor ($=V/u_*$).

## References


ASCE Task Committee on Hydraulics, Bank Mechanics and Modeling of River Width Adjustment. (1998). "River width adjustment. I: Processes and mechanisms." *J. Hydraul. Eng.*, 124(9), 881–902.

Ashmore, P. E. (1982). "Laboratory modeling of gravel braided stream morphology." *Earth Surf. Processes Landforms*, 7, 201–225.

Ashmore, P. E. (1988). "Bed load transport in braided gravel-bed stream models." *Earth Surf. Processes Landforms*, 13, 677–695.

Ashmore, P. E. (1991). "How do gravel-bed rivers braid?" *Can. J. Earth Sci.*, 28, 326–341.

Ashmore, P. E. (2001). "Braiding phenomena: statics and kinestics." *Gravel-bed rivers V*, M. P. Mosley, ed., New Zealand Hydrological Society, Wellington, New Zealand, 95–114.

Blondeaux, P., and Seminara, G. (1985). "A unified bar-bend theory of river meanders." *J. Fluid Mech.*, 157, 449–470.

Bradford, S. F., and Sanders, B. F. (2002). "Finite-volume model for shallow-water flooding of arbitrary topography." *J. Hydraul. Eng.*, 128(3), 289–298.

Darby, S. E., Alabyan, A. E., and Van de Wiel, M. J. (2002). "Numerical simulation of bank erosion and channel migration in meandering rivers." *Water Resour. Res.*, 38(9), 1163.

Darby, S. E., and Thorne, C. R. (1996). "Numerical simulation of widening and bed deformation of straight sand-bed rivers. I: Model development." *J. Hydraul. Eng.*, 122(4), 184–193.

Darby, S. E., and Thorne, C. R., and Simon, A. (1996). "Numerical simulation of widening and bed deformation of straight sand-bed rivers. II: Model evaluation." *J. Hydraul. Eng.*, 122(4), 194–202.

Engelund, F. (1974). "Flow and bed topography in channel beds." *J. Hydraul. Div., Am. Soc. Civ. Eng.*, 100(11), 1631–1648.

Enggrob, H. G., and Tjerry, S. (1999). "Simulation of morphological characteristics of a braided river." *IAHR Symp. on River, Coastal, and Estuarine Morphodynamics*, IAHR, Genova, Italy, 585–594.

Federici, B., and Paola, C. (2003). "Dynamics of channel bifurcations in noncohesive sediments." *Water Resour. Res.*, 39(6), 1162.

Fujita, Y. (1989). "Bar and channel formation in braided streams." *River meandering*, S. Ikeda and G. Parker, eds., AGU Water Resources Monograph, 12, 417–462.

Hasegawa, K. (1984). "Hydraulic research on planimetric forms, bed topographies and flow in alluvial rivers." PhD dissertation, Hokkaido Univ., Sapporo, Japan (in Japanese).

Hoey, T. B., and Sutherland, A. J. (1991). "Channel morphology and bedload pulses in braided rivers: a laboratory study." *Earth Surf. Processes Landforms*, 16, 447–462.

Ikeda, S., Parker, G., and Sawai, K. (1981). "Bend theory of river meanders. Part 1. Linear development." *J. Fluid Mech.*, 112, 363–377.

Iwagaki, Y. (1956). "Hydrodynamical study on critical tractive force." *Proc., JSCE*, 41, 1–21 (in Japanese).

Kishi, T., and Kuroki, M. (1973). "Bed form and flow resistance in alluvial rivers (I)." *Research Rep.*, Faculty of Engineering, Hokkaido Univ., 67, 1–23 (in Japanese).

Kovacs, A., and Parker, G. (1994). "A new vectorial bedload formulation and its application to the time evolution of straight river channels." *J. Fluid Mech.*, 267, 153–183.

Kuroki, M., and Kishi, T. (1984). "Regime criteria on bars and braids in alluvial straight channels." *Proc., JSCE*, 342, 87–96 (in Japanese).

Leopold, L. B., and Wolman, M. G. (1957). "River channel patterns: braided, meandering and straight." *U.S. Geol. Surv. Prof. Pap.*, 282-B, 39–84.

McArdell, B. W., and Faeh, R. (2001). "A computational investigation of river braiding." *Gravel-bed rivers V*, M. P. Mosley, ed., New Zealand Hydrological Society, Wellington, New Zealand, 73–86.

Meyer-Peter, E., and Muller, R. (1948). "Formulas for bed-load transport." *Proc., 2nd Congress*, IAHR, Stockholm, Sweden, 2(2), 39–64.

Murray, A. B., and Paola, C. (1994). "A cellular model of braided rivers." *Nature (London)*, 371, 54–57.
Murray, A. B., and Paola, C. (1997). "Properties of a cellular braided-stream model." *Earth Surf. Processes Landforms*, 22, 1001–1025.
Nagata, N., Hosoda, T., and Muramoto, Y. (2000). "Numerical analysis of river channel processes with bank erosion." *J. Hydraul. Eng.*, 126(4), 243–252.
Parker, G., Sawai, K., and Ikeda, S. (1982). "Bend theory of river meanders. Part 2. Nonlinear deformation of finite-amplitude bends." *J. Fluid Mech.*, 115, 303–314.
Pizzuto, J. E. (1990). "Numerical simulation of gravel river widening." *Water Resour. Res.*, 26(9), 1971–1980.
Shimizu, Y. (2002). "A method for simultaneous computation of bed and bank deformation of a river." *River Flow 2002, Int. Conf. on Fluvial Hydraulics*, Louvain-la-Neuve, Belgium, 793–801.
Shimizu, Y., Hirano, N., and Watanabe, Y. (1996). "Numerical calculation of bank erosion and free meandering." *Annu. J. Hydr. Engrg., JSCE*, 40, 921–926 (in Japanese).
Shimizu, Y., Kurabayashi, H., and Fujita, M. (2001). "Numerical calculation of bed deformation in braided stream." *Annu. J. Hydr. Engrg., JSCE*, 45, 739–744 (in Japanese).
Sun, T., Meakin, P., and Jossang, T. (2001a). "A computer model for meandering rivers with multiple bed load sediment sized, 1, Theory." *Water Resour. Res.*, 37(8), 2227–2241.
Sun, T., Meakin, P., and Jossang, T. (2001b). "A computer model for meandering rivers with multiple bed load sediment sized, 2, Computer simulations." *Water Resour. Res.*, 37(8), 2243–2258.
Watanabe, A., Fukuoka, S., Yasutake, Y., and Kawaguchi, H. (2001). "Groin arrangements made of natural willows for reducing bed deformation in a curved channel." *Adv. River Eng.*, 7, 285–290 (in Japanese).
Yabe, T., and Aoki, T. (1991). "A universal solver for hyperbolic equations by cubic-polynomial interpolation I. One-dimensional solver." *Comput. Phys. Commun.*, 66, 219–232.
Yabe, T., Ishikawa, T., Kadota, Y., and Ikeda, F. (1990). "A numerical cubic-interpolated pseudoparticle (CIP) method without time splitting technique for hyperbolic equations." *J. Phys. Soc. Jpn.*, 59(7), 2301–2304.
Yabe, T., Ishikawa, T., Wang, P. Y., Aoki, T., Kadota, Y., and Ikeda, F. (1991). "A universal solver for hyperbolic equations by cubic-polynomial interpolation II. Two and three-dimensional solvers." *Comput. Phys. Commun.*, 66, 233–242.
Zhao, D. H., Shen, H. W., Tabios, G. Q., III, Lai, J. S., and Tan, W. Y. (1994). "Finite-volume two-dimensional unsteady-flow model for river basins." *J. Hydraul. Eng.*, 120(7), 863–883.